Available online at www.sciencedirect.com
SCIENCE DIRECT
Journal of Catalysis 240 (2006) 182–193
JOURNAL OF CATALYSIS
www.elsevier.com/locate/jcat

The effects of Fe on the oxygen storage and release properties of model Pd–Rh/CeO_2–Al_2O_3 three-way catalyst

Panayiota S. Lambrou, Angelos M. Efstathiou *

Department of Chemistry, Heterogeneous Catalysis Laboratory, University of Cyprus, P.O. Box 20537, CY 1678 Nicosia, Cyprus

Received 31 December 2005; revised 23 March 2006; accepted 24 March 2006

Available online 27 April 2006

Abstract

This work attempts to gain fundamental information about the role of Fe in the chemical deactivation of a three-way catalyst (TWC), with Fe originating from materials used in the construction of automotive engines and exhaust pipe systems. Topics of particular interest are Fe's role as a chemical poison of the oxygen storage and release properties of a model TWC (1 wt% Pd–Rh/20 wt% CeO_2–Al_2O_3), its effects on the redox properties of Pd and Rh, and its effects on NO and CO chemisorption; these topics are investigated for the first time here. Oxygen storage capacity (OSC) measurements in the 500–850 °C range indicated that OSC increased after the addition of 0.1–0.3 wt% Fe in the model catalyst. It can be concluded that iron acted as an oxygen storage component under oxidizing conditions through the process Fe → FeO → Fe_3O_4 ($FeO{\cdot}Fe_2O_3$) → Fe_2O_3, and not as a chemical poison of the oxygen storage and release properties of the solid. However, when the amount of deposited iron increased to 0.4 wt%, the OSC of the catalyst deteriorated but still remained slightly greater than that measured over the catalyst uncontaminated with Fe catalyst. H_2 temperature-programmed desorption and reduction and X-ray photoelectron spectroscopy (XPS) studies performed on the oxidized and reduced Fe-contaminated samples indicated that iron (0.1–0.3 wt%) was deposited on both noble metals (Pd and Rh) and support, causing the development of electronic interactions that influenced the oxidation states of Pd and Rh and enhanced the oxygen chemisorption properties of ceria. In situ diffuse reflectance infrared Fourier transform spectroscopy (DRIFTS) studies proved that iron deposited to a level of 0.2 wt% significantly favors the formation of a superoxide (O_2^-) species on CeO_2. The latter species was found to desorb completely at temperatures above 250 °C. However, at the 0.4 wt% level, O_2^- formation was minor. In situ DRIFTS chemisorption studies of CO and NO performed at 25 °C also provided important information about the electronic interactions between Pd and Fe in the model Pd–Rh–Fe/20 wt% CeO_2–Al_2O_3 TWC, confirming the XPS results.

Keywords: TWC deactivation; Iron; OSC; In situ DRIFTS; XPS; Transient kinetics; Oxygen isotopic exchange; H_2 TPD; H_2 TPR

1. Introduction

It is well known that commercial three-way catalysts (TWCs) lose their activity and performance (deactivation phenomenon) after about 150,000 km as a result of various changes to which their structure and surface chemical state are subjected [1–3]. TWC deactivation can be categorized into three main groups: chemical [1], thermal [4–6], and mechanical. Chemical deactivation is considered the most complex of the three processes. When attempting to prolong catalyst life, resistance to chemical deactivation is one of the most important problems that must be overcome. This is because chemical deactivation is proportional to the operational time, whereas thermal effects decay exponentially over time [7].

Various chemical compounds (i.e., impurities) present in automotive engine exhaust gas can strongly interact chemically with the active sites of TWCs, decreasing its activity and overall performance. A metal contaminant can poison active sites through deposition mechanisms (geometric effect) or can alter the adsorptive properties of an active site or a catalyst component (electronic effect) [8]. Another possibility is modification of the chemical nature of active sites by the creation of new phases that can change the catalytic performance of TWCs. The most common contaminants retraced from aged commercial TWCs are Pb and S originating from fuel additive components

* Corresponding author. Fax: +35722 892801.
E-mail address: efstath@ucy.ac.cy (A.M. Efstathiou).

0021-9517/$ – see front matter
doi:10.1016/j.jcat.2006.03.014

[9–11]; P, Zn, and Ca from lubricant oil additives [3,12,13]; and Fe, Ni, Cu, and Cr from the materials used to construct engine and exhaust pipe systems [14–16].

Many researchers have detected the presence of Fe on aged commercial TWCs. Angelidis et al. [15,16] reported that Fe was present on aged TWCs of various origins and mileages at concentrations in the 0.08–2.0 wt% range. Tabata et al. [7] detected iron at the level of 0.41 wt% among other contaminants in an aged TWC. Iron, among other contaminants (e.g., Pb, Ni, Ca, P), has been detected by inductively coupled plasma (ICP) and total X-ray fluorescence on commercial TWCs of varying ages (59, 96, and 242 $\times 10^3$ km) [13,17].

To our knowledge, only Tabata et al. [7] have prepared model Fe-contaminated TWCs in an attempt to interpret the observed decrease in N_2 selectivity of the NO reduction over aged TWCs for natural gas-fueled engines. Iron detected at the surface of the catalyst washcoat layer was considered to poison Rh and/or other active metals, but not to reduce the selectivity to N_2 formation of the NO reduction [7]. Iron was used as a promoter mainly of the water–gas shift (WGS) reaction and to a lesser extent of other catalytic reactions [18–20]. For example, Wang and Gorte [20] showed that Fe-promoted Pd/CeO_2 catalysts resulted in higher (by a factor of eight) WGS reaction rates compared with other promoters (Y, Tb, and Gd).

Sirijaruphan et al. [21] studied the selective oxidation of CO in the presence of H_2 over Pt/γ-Al_2O_3 and found that deposition of Fe enhanced the intrinsic site reactivity, possibly due to the formation of new oxygen adsorption sites and/or an increase in oxygen coverage. In another study, Pt–Fe alloy particles supported on alumina were found to prevent Pt sintering [18]. Mastelaro et al. [22] doped ZrO_2–CeO_2 systems with Fe and Ni in an attempt to better understand the tetragonal phase stabilization process of zirconia. Using extended X-ray absorption fine structure (EXAFS) studies, they clearly showed that Fe atoms formed a solid solution only with ZrO_2, thereby introducing oxygen vacancies in the oxide lattice, which in turn enhanced oxygen diffusion and improved the tetragonal-phase ZrO_2 stabilization process.

The present work aimed to investigate for the first time the effects of low loading of Fe (0.1–0.4 wt%) on the oxygen storage and release properties of TWCs, with Fe present as a chemical contaminant of TWC. Model TWCs consisting of 1 wt% Pd–Rh (14/1)/20 wt% CeO_2–Al_2O_3 and impregnated with varying Fe loadings (0.1–0.4 wt%) were used. The effects of Fe_2O_3 (3.3–13.2 wt%) used as component of an Al_2O_3–CeO_2 support, the latter impregnated with Pt and Ba on the NO_x storage reduction catalyst, were studied [23]. The OSC of the catalyst was found to depend linearly on the iron oxide loading.

In the present work, X-ray photoelectron spectroscopy (XPS) studies performed after various oxidation and reduction treatments on the Fe-contaminated and uncontaminated model catalysts, along with in situ diffuse reflectance infrared Fourier transform spectroscopy (DRIFTS) chemisorption studies of CO and NO, were used to investigate the oxidation states of Pd and Rh in the presence of Fe. In addition, H_2 temperature-programmed desorption (TPD) and temperature-programmed reaction (TPR) studies were conducted to investigate the effect of Fe on the chemisorptive and reducing properties of the model catalyst. Fe's effect on the thermal stability and exchange of superoxide adsorbed species (O_2^-) populated mainly on CeO_2 in the Pd–Rh–Fe/CeO_2–Al_2O_3 catalysts were studied by in situ DRIFTS using $^{18}O_2$.

2. Experimental

2.1. Model TWCs

A model three-way catalyst, 1 wt% Pd–Rh (14/1)/20 wt% CeO_2–Al_2O_3, was prepared as follows. The support material was prepared by impregnating γ-Al_2O_3 (Aldrich, standard grade) with $Ce(NO_3)_3{\cdot}6H_2O$ (Aldrich, 99.999%) in distilled deionized water at 40 °C so as to yield 20 wt% CeO_2–Al_2O_3. After drying at 120 °C for 12 h, the support material was calcined in air at 200–800 °C with a 1-h stay at every 100 °C increment. The CeO_2–Al_2O_3 support was then impregnated with appropriate amounts of $Rh(NO_3)_3$ and $Pd(NO_3)_2$ (Aldrich, 99.999%) in distilled deionized water at 40 °C so as to yield 1 wt% total metal loading (Pd/Rh = 14/1). The resulting solid was then dried at 120 °C for 12 h. Portions of the 1 wt% Pd–Rh/20 wt% CeO_2–Al_2O_3 solid were impregnated with appropriate amounts of $Fe(NO_3)_3$ (Aldrich, 99.99%) so as to yield iron loadings in the 0.1–0.4 wt% range. After drying at 120 °C for 12 h, the solids were stored without further treatment. Herein the 1 wt% Pd–Rh/20 wt% CeO_2–Al_2O_3 solid is referred to as PRCA; the 20 wt% CeO_2–Al_2O_3 solid support, as CA.

2.2. OSC measurements

2.2.1. Pulse injection technique

The OSC of the various model TWCs (with or without Fe) was measured by the pulse injection technique as described previously [2,24,25]. The reactive oxygen species present in a model TWC sample is defined as the amount of H_2 or CO consumed (consecutive pulses) when H_2 or CO is used to titrate the oxygen species, or the amount of oxygen consumed during the reoxidation stage [2]. The latter amount is referred to as oxygen storage capacity complete (OSCC). The amount of the most reactive oxygen (labile oxygen) of the catalyst is defined as the amount of oxygen that reacts during the first H_2 or CO pulse and referred to as the OSC. Before any OSC measurements were obtained, the catalyst sample (50 mg) was oxidized (20% O_2/He) at 700 °C for 2 h and then reduced (1 bar H_2) at 300 °C for 2 h. It was then pretreated in a 20% O_2/He gas mixture for 1 h at a given temperature, T_{OSC} [2]. The transient flow system, the microreactor, and the mass spectrometer were as described previously [25,26].

The OSC of the uncontaminated and Fe-contaminated catalysts was also measured at 500 °C after 2 h of oxidation (20% O_2/He) at 500 °C, followed by 2 h of reduction (1 bar H_2) at 600 °C. The latter high-temperature reduction step was used to increase the oxygen vacancies on the surface and in the bulk of the CeO_2 support component.

Table 1
Description of step gas concentration switches for dynamic oxygen storage capacity (DOSC) measurements[a]

Type of experiment	Sequence of step gas concentration switches
A	1.5% O_2/He (T_{OSC}, 30 s) →He (T_{OSC}, 30 s) → 3% CO/3% Ar/He (T_{OSC}, 300 s), repeat cycle
B	10% CO_2/1.5% O_2/He (T_{OSC}, 30 s) → He (T_{OSC}, 30 s) → 3% CO/3% Ar/He (T_{OSC}, 300 s), repeat cycle

[a] The underlined step in the sequence of step gas concentration switches indicates that estimation of DOSC was based on this step.

2.2.2. Alternating-step gas concentration switches

Experiment A was conducted to measure OSC by alternating step concentration switches of the gas composition (dynamic oxygen storage capacity [DOSC]); the findings are reported in Table 1. The catalyst sample (50 mg) was initially pretreated in 20% O_2/He for 1 h at a given temperature, T_{OSC}. Ar was present in the reducing gas to record the transient response of a nonadsorbing and nonreacting gas passing from the switching valve through the reactor (with the catalyst in place) to the mass spectrometer, to evaluate CO consumption due to reaction and chemisorption [25,27].

Experiment B was conducted to study how the presence of CO_2 in the oxidizing gas mixture affects DOSC; the results are presented in Table 1. The O_2 and CO_2 concentrations used were similar to those found in the exhaust gas of a gasoline-powered automobile. The total flow rate used in all of the DOSC experiments was 30 NmL/min. The accuracy of OSC and DOSC measurements was within 5%.

2.3. TPD and TPR experiments

H_2 TPD and H_2 TPR experiments were conducted in a specially designed gas flow system as described previously [26]. A 0.3-g catalyst sample and a 30-NmL/min total flow rate were used. Chemical analysis of the reactor's gas effluent stream was done with an on-line quadrupole mass spectrometer (Omnistar, Balzers) equipped with a fast-response inlet capillary/leak valve (SVI 050, Balzers) and data acquisition system. The gaseous responses obtained by mass spectrometry were calibrated against standard mixtures. For H_2 TPD runs, the fresh catalyst sample was first oxidized in 20% O_2/He at 700 °C for 2 h, and then reduced in 10% H_2/He at 300 °C for 2 h. The catalyst was purged in He flow at 500 °C until no H_2 evolution was observed, then cooled quickly to room temperature for H_2 chemisorption followed by TPD ($\beta = 30$ °C/min up to 825 °C).

For the H_2 TPR experiments, after catalyst pretreatment in 20% O_2/He at 500 °C for 2 h, the feed was changed to He for 15 min and the reactor was rapidly cooled to 25 °C in He flow. A 2% H_2/He gas mixture was then switched to the reactor, and the temperature of the catalyst was increased to 825 °C at a rate of 30 °C/min. The mass numbers (m/z) 2, 18, and 32 were used for H_2, H_2O, and O_2, respectively. The accuracy of quantitative analyses of the TPD and TPR response curves was within 5%.

2.4. XPS

X-Ray photoelectron spectroscopy (XPS) studies were performed with a VG Escalab 200R spectrometer equipped with a hemispherical electron analyzer and an Mg-K_α (1253.6 eV) X-ray source. The sample was placed in a copper holder mounted on a sample rod in the pretreatment chamber of the spectrometer, then outgassed at room temperature for 1 h. A certain region of the XPS spectrum was then scanned a number of times, to obtain a good signal-to-noise ratio. The binding energies were referenced to the spurious C 1s peak (284.6 eV) used as internal standard to take the charging effects into account. The areas of the peaks were computed by fitting the experimental spectra to Gaussian/Lorenztian curves after removal of the background (Shirley function). Surface atom ratios were calculated from peak area ratios normalized by using the corresponding atomic sensitivity factors [28].

2.5. In situ DRIFTS studies

In situ DRIFTS studies were performed using a high-pressure DRIFTS cell equipped with CaF_2 windows. Catalyst sample (∼30 mg) in a fine-powder form was well mixed with KBr (1:10 w/w) and placed firmly into the ceramic cup of the DRIFTS cell (Spectra Tech). Spectra were recorded using a Perkin–Elmer Spectrum GX II FTIR spectrometer interfaced with a computer. All spectra were recorded as a single background beam experiment. The ratio of the spectrum was then taken with respect to a background spectrum recorded under Ar flow at the temperature of the experiment. The spectral resolution used was 2 cm^{-1}. Before the measurements were taken, the sample was pretreated in 20% O_2/Ar at 550 °C for 2 h, followed by reduction in 10% H_2/Ar at 300 °C for 2 h. To further increase the number of oxygen vacancies in the CeO_2 solid, the catalyst sample was reduced in situ in a 20% H_2/Ar mixture at 600 °C for 2 h.

O_2 TPD was performed after a 30-min oxygen treatment of the catalyst with 3% $^{16}O_2$/Ar at 25 °C. The DRIFTS cell was then purged with Ar for 15 min, and the temperature was increased to 550 °C. Infrared (IR) spectra were recorded every 100 °C in the 3500–800 cm^{-1} range. Oxygen isotopic exchange was performed at 25 °C. After 30 min of adsorption in 3% $^{16}O_2$/Ar gas mixture, the feed was switched to Ar for 10 min, followed by a switch to 3% $^{18}O_2$/Ar. Exchange of the adsorbed surface oxygen species with $^{18}O_2$ was followed by DRIFTS after 2, 5, and 10 min on the isotopic gas mixture. Every IR spectrum presented here corresponds only to the spectrum of the adsorbed phase (the spectrum of the solid itself was subtracted).

CO and NO chemisorption studies were also performed at 25 °C on the PRCA and 0.2 wt% Fe/PRCA catalysts. Before any measurements, the sample was pretreated in 20% O_2/Ar at 550 °C for 2 h, followed by reduction in 10% H_2/He at 300 °C for 2 h. The DRIFTS cell was then purged with Ar and

cooled to 25 °C. The concentrations of CO and NO used were 5 and 1 vol%, respectively, with Ar as a balance gas.

3. Results and discussion

3.1. OSC measurements

3.1.1. Pulse injection technique

Fig. 1 presents results of OSCC and OSC measurements (μmol-O/g_{cat}) obtained over the x wt% Fe/PRCA ($x = 0$, 0.1, 0.2, 0.3, and 0.4) catalysts in the 500–850 °C (T_{OSC}) range using H_2 (Fig. 1a) and CO (Fig. 1b) as reducing agents. The OSC and OSCC increased with increasing temperature at which oxygen was stored and reduced in H_2 (T_{OSC}). This is an expected behavior considering the fact that the kinetic rate constant (k) of the reduction of oxygen species present in PdO, Rh_2O_3, Fe_2O_3, and CeO_2 is expected to increase with increasing temperature. In addition, by increasing the temperature under which oxygen is stored mainly in the bulk of CeO_2, the amount of this stored oxygen is expected to increase. It was found that the OSCC of the five catalysts investigated increased from 41 to 54% on increasing the T_{OSC} from 500 to 850 °C (Fig. 1a).

An important result presented in Fig. 1 is that by increasing the Fe loading in the 0.1–0.3 wt% range, the OSC and OSCC increase. These results suggest that Fe deposited in the PRCA catalyst either acts as an additional oxygen storage component or alters the oxygen chemisorptive properties of Pd–Rh/CeO_2 and/or CeO_2 solid surfaces, which are associated with the oxygen storage and release processes. A possible interpretation of these results might be that iron present in the catalyst is first oxidized to Fe_2O_3 after the 1-h treatment in 20% O_2/He at T_{OSC} (oxygen storage step). Then, during the reduction step (H_2 pulses), in addition to the oxygen stored in the metals (PdO and Rh_2O_3) and CeO_2 support, oxygen of the iron oxide formed can also be reduced and measured. Thus, the latter provides greater OSC and OSCC than those obtained in the PRCA catalyst uncontaminated with iron. The OSC of iron oxide was determined by performing similar OSC measurements on commercial Fe_2O_3 (Aldrich, 99.98%). The fact that iron oxide can store oxygen in the 500–850 °C range has to do with the multiple oxidation states of Fe, where Fe_2O_{3-x} (a nonstoichiometric oxide) can store oxygen under oxidizing conditions and release it under reducing conditions [20]. On the other hand, the amount of oxygen (μmol-O/g) stored in the iron oxide corresponding to 0.3 wt% Fe deposited in PRCA is 80 μmol-O/g, quantity that cannot explain the increased OSCC observed in Figs. 1a and 1b. For example, at 700 °C (T_{OSC}), the OSCC of PRCA was found to be 208 μmol-O/g, compared to 345 μmol-O/g of the 0.3 wt% Fe/PRCA. In other words, a 26% increase in OSCC is estimated (after subtracting the contribution of Fe_2O_3, if the latter was fully reduced by H_2 pulses at 700 °C). Furthermore, if the additional OSCC were the result of OSCC due to the iron alone, then a monotonic increase in OSCC with increasing Fe loading in the 0–0.4 wt% range would be expected, a result not seen in Fig. 1. This strongly implies that iron should have additional effects on the chemistry involved in the oxygen storage and release processes.

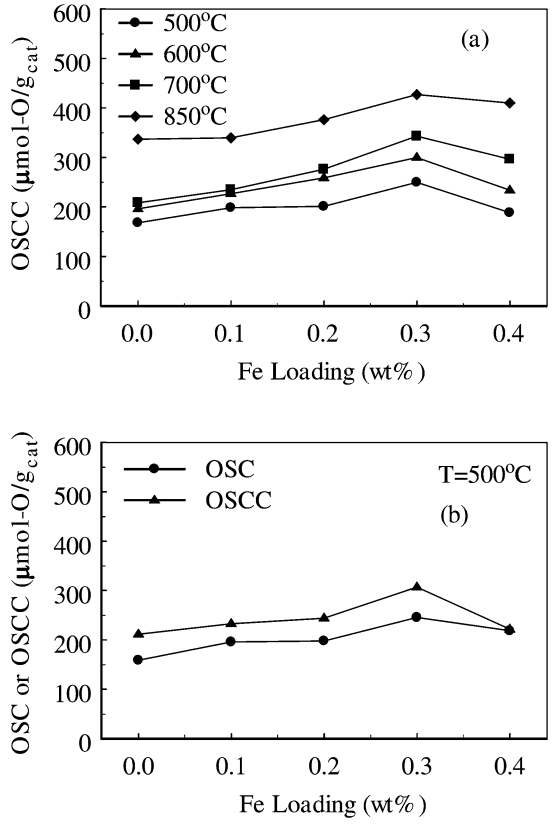

Fig. 1. OSC and OSCC (μmol-O/g_{cat}) measured by H_2/O_2 (a) and CO/O_2 (b) pulsed-feed experiments over the x wt% Fe/PRCA ($x = 0$, 0.1, 0.2, 0.3, and 0.4) solids in the 500–850 °C range.

Yamazaki et al. [23] showed that at 300 °C there was a good linear correlation between OSC and Fe_2O_3 loading in the 3.3–13.2 wt% range for the Pt–Ba/Al_2O_3–CeO_2–Fe_2O_3 catalyst. They proposed that iron oxides contributed to the OSC of the solid independently by the following reaction scheme:

$$Fe + (1/2)O_2 \leftrightarrow FeO, \quad (1)$$

$$3FeO + (1/2)O_2 \leftrightarrow Fe_3O_4, \quad (2)$$

$$2Fe_3O_4 + (1/2)O_2 \leftrightarrow 3Fe_2O_3. \quad (3)$$

Based on reactions (1)–(3) and the fact that the iron oxide was initially present in the support material on which Pt was deposited, an increased OSC with increasing iron oxide loading can be reasonably expected. However, in the present work, iron was deposited by wet impregnation in the Pd–Rh/Al_2O_3–CeO_2 solid in small amounts (0.4 wt%). Some intrinsic reasons why the increased Fe loading in the 0.1–0.4 wt% range does not have a monotonic positive effect on the OSC of the present catalytic system are discussed later in the paper. Figs. 1a and 1b illustrate that even though deposition of 0.4 wt% Fe in PRCA catalyst leads to decreased OSC and OSCC compared with those obtained on the 0.3 wt% Fe/PRCA, the former values are not lower than those measured over the PRCA catalyst.

Fig. 2 presents OSCC (μmol-O/g_{cat}) measured at T_{OSC} = 500 °C over the x wt% Fe/PRCA ($x = 0$, 0.1, 0.2, 0.3, and 0.4) catalysts after high-temperature reduction ($T_{red} = 600$ °C) (see

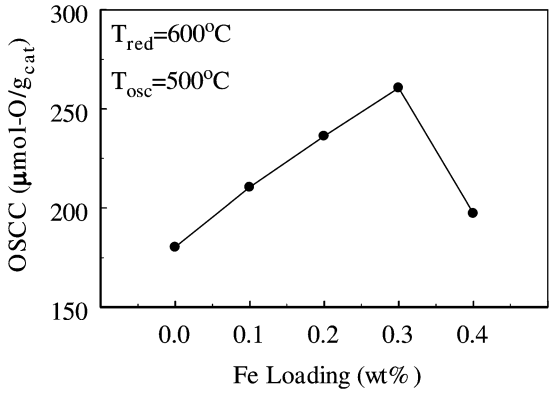

Fig. 2. OSCC (μmol-O/g_{cat}) measured by H_2/O_2 pulsed-feed experiments at 500 °C over the x wt% Fe/PRCA ($x = 0$, 0.1, 0.2, 0.3, and 0.4) solids after H_2 reduction (1 bar) at 600 °C for 2 h (see Section 2.2.1).

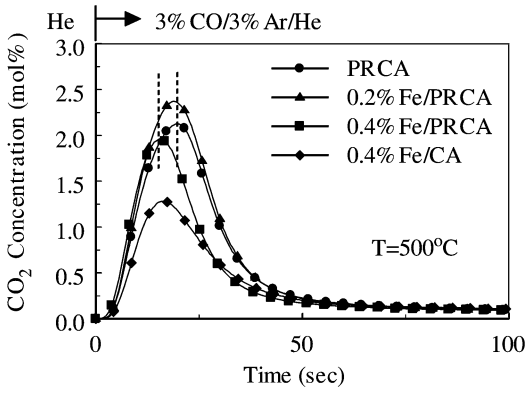

Fig. 3. Transient response curves of CO_2 obtained over the PRCA, 0.2 and 0.4 wt% Fe/PRCA, and 0.4 wt% Fe/CA solids at 500 °C according to the gas delivery sequence: 1.5% O_2/He (T_{OSC}, 30 s) → He (T_{OSC}, 30 s) → 3% CO/3% Ar/He (T_{OSC}, 300 s), repeat cycle (see also Table 1).

Section 2.2.1). As clearly shown, OSCC increased after the deposition of 0.1–0.3 wt% Fe but decreased after the addition of 0.4 wt% Fe, in agreement with the findings at $T_{red} = 300$ °C (Fig. 1). In addition, the OSCC measured at the same temperature ($T_{OSC} = 500$ °C) in both experiments Figs. 1a and 2 was 4.0–14.7% greater (depending on Fe loading used) after the high-temperature reduction ($T_{red} = 600$ °C) of ceria.

3.1.2. Alternating step gas concentration switches/dynamic OSC measurements

Fig. 3 presents transient response curves of CO_2 obtained over the x wt% Fe/PRCA ($x = 0$, 0.2, and 0.4) and 0.4 wt% Fe/CA solids obtained at 500 °C under DOSC measurements (experiment A in Table 1). The greatest amount of CO_2 was produced with the 0.2 wt% Fe/PRCA; the lowest, with the 0.4 wt% Fe/PRCA solid. The latter results agree with those obtained using the pulse injection technique (Fig. 1). The peak maximum position of the transient response curve of CO_2 obtained over the 0.4 wt% Fe/PRCA shifted to lower reaction times (by 8 s) compared with that obtained over the PRCA solid. This shift (noted by vertical dashed line segments in Fig. 3) was earlier explained to be associated with the rate constant (k_2) of the back-spillover of oxygen process and not with the rate constant (k_1) of CO oxidation step occurring on the Pd and Rh metal surfaces [25,29]. Therefore, it is concluded that even though addition of iron (0.4 wt%) in PRCA increases the amount of oxygen stored in Fe/PRCA, a negative effect on the site reactivity (k_2) associated with labile oxygen diffusion in ceria is obtained, the latter being one of the "oxygen storage" materials of the washcoat of TWC. As will be shown later by XPS studies, some Fe is found in close contact with Pd and Rh crystallites. As the amount of deposited Fe increases, partial coverage of Pd and Rh might be expected, which seems to affect the rate of oxygen back-spillover from ceria to the noble metals.

When 10% CO_2 was added in the O_2/He feed gas stream (Table 1, experiment B), the amount of CO_2 produced decreased compared with that corresponding to the results in Fig. 3 (no CO_2 was present in the oxidizing gas mixture), except for the 0.4 wt% Fe/CA solid (Table 2). Formation of stable carbonate species at 500 °C under the experimental conditions can

Table 2
Amounts of CO consumed and CO_2 produced (μmol/g) after 300 s in the 3% CO/3% Ar/He gas mixture at 500 °C during experiments A and B (Table 1)

Type of experiment	Catalyst	CO consumption (μmol/g)	CO_2 production (μmol/g)	λ = [CO cons.]/[CO_2 prod.]
A	PRCA	300	273	1.1
	0.2 wt% Fe/PRCA	312	290	1.03
	0.4 wt% Fe/PRCA	241	239	1.0
	0.4 wt% Fe/CA	160	158	1.0
B	PRCA	293	237	1.2
	0.2 wt% Fe/PRCA	312	276	1.1
	0.4 wt% Fe/PRCA	290	192	1.5
	0.4 wt% Fe/CA	197	150	1.3

explain these results. These species poison oxygen storage sites in CeO_2 [30]. This explanation is supported by the experimental findings in this work. A similar transient experiment to that reported in Fig. 3 was performed using the DRIFTS cell as reactor, with the carbonate band region scanned every 5 s. The area bands due to the carbonates associated with ceria were clearly observed to increase after the switch from Ar to O_2/CO_2/Ar. In addition, CO pulse-feed experiments similar to those reported in Fig. 1 indicated IR bands due to adsorbed carbonate species. Table 2 reports values of the λ parameter (defined as the ratio of the amount of CO consumed to that of CO_2 produced) according to the experiments of Fig. 3 and also in the presence of CO_2 in the oxidizing gas mixture (experiment B in Table 1). Note that λ takes values equal to unity when only the following reactions occur:

$$CO(g) + O\text{–}S_1 \rightarrow CO_2(g) + S_1, \quad (4)$$

$$O\text{–}S_2 + S_1 \rightarrow O\text{–}S_1 + S_2 \quad \text{(oxygen back-spillover)}, \quad (5)$$

$$CO(g) + OH\text{–}S_2 \rightarrow CO_2(g) + (1/2)H_2(g) + S_2. \quad (6)$$

Here S_1 refers to a site on the precious metal/metal oxide, and S_2 is a site on the ceria–alumina support. But reaction (6) must be excluded, because no H_2 production was observed. When λ takes values larger than unity, other side reactions must occur, for example, adsorption of CO_2 and disproportionation of CO

to give C or Fe_3C and CO_2. All catalysts exhibited λ values close to unity in experiment A (Fig. 3), whereas the opposite was true in experiment B (i.e., λ values were larger than unity; see Table 2).

3.2. H_2 TPD

Fig. 4 presents H_2 TPD response curves obtained on the x wt% Fe/PRCA ($x = 0$, 0.2, and 0.4) and 0.4 wt% Fe/CA solids. In the case of PRCA (curve A), the amount of H_2 desorbed was 40.9 μmol-H/g_{cat}. Addition of 0.2 and 0.4 wt% Fe in PRCA caused 24.0 and 20.7% increases, respectively, in the amount of H_2 desorbed, but the shape and position of H_2 desorption peaks were largely different. The H_2 TPD response curve of PRCA consists of one peak centered at $T_M = 200\,^\circ$C with a large shoulder at the falling part of the curve and a smaller shoulder at the rising part. Addition of 0.2 wt% Fe caused the T_M to shift to higher values ($T_M = 250\,^\circ$C, curve B), with the shoulder observed at the rising part of the desorption peak becoming larger compared with that seen in the PRCA catalyst. With a further increase in Fe content to 0.4 wt%, the high-temperature side of the desorption peak (curve C) remained practically the same as that observed in the 0.2 wt% Fe/PRCA and 0.4 wt% Fe/CA solids. These results strongly suggest that Fe affected the desorption kinetics of H_2 associated with the Pd surface (Pd/Rh = 14:1). As demonstrated by the H_2 TPR and XPS measurements, the electronic environment of the Pd surface atoms was altered due to the presence of Fe, thus affecting their chemisorptive properties. Formation of Fe–Pd alloy has been reported under reducing conditions (i.e., strong interaction of Fe^0 and Pd^0) [31,32], with the Pd–Fe phase diagram showing Pd and Fe forming a single-phase $PdFe_x$ alloy ($0 < x < 0.12$) [33].

3.3. H_2 TPR studies

H_2 TPR traces obtained over the x wt% Fe/PRCA ($x = 0$ and 0.2) and 0.2 wt% Fe/CA solids are shown in Fig. 5a, and corresponding traces obtained on the x wt% Fe/PRCA ($x = 0$ and 0.4) and 0.4 wt% Fe/CA solids are shown in Fig. 5b. The H_2 TPR traces thus obtained exhibit two resolved peaks in significantly different temperature ranges. The first peak, located in the 25–225 °C range can be attributed mainly to reduction of rhodium and palladium oxides. In particular, the peaks centered at 45 °C (curve A) and 85 °C (curve B) in Fig. 5a are attributed to reduction of Rh_2O_3 and PdO oxides [24,34–38]. The peaks appearing in the 200–450 °C range can be attributed to the reduction of metal oxides in close contact with CeO_2 (Rh–O–Ce and Pd–O–Ce bonds) [39,40], whereas the H_2 TPR trace in the 450–825 °C range can be attributed to bulk reduction of CeO_2 [34].

The reduction of iron oxide involves a two-step process, with Fe_2O_3 first reduced to Fe_3O_4 ($FeO{\cdot}Fe_2O_3$) and then to metallic Fe [41]. The H_2 TPR trace of Fe_2O_3 to Fe_3O_4 appears in the 285–420 °C range; that of Fe_2O_3 to Fe^0, in the 300–480 °C range [42]. Unmuth et al. [43] reported that the H_2 TPR trace of 5 wt% Fe/SiO_2 consists of two peaks ($T_M = 307$ and 447 °C), which correspond to the aforementioned two-step reduction process. Munteanu et al. [44] reported that the TPR trace of α-Fe_2O_3 also comprises two peaks ($T_M = 280$ and 427 °C). The peak at 280 °C with a shoulder was ascribed to the reduction of Fe_2O_3 (hematite) to Fe_3O_4 (magnetite),

$$3Fe_2O_3 + H_2 \rightarrow 2Fe_3O_4 + H_2O, \quad (7)$$

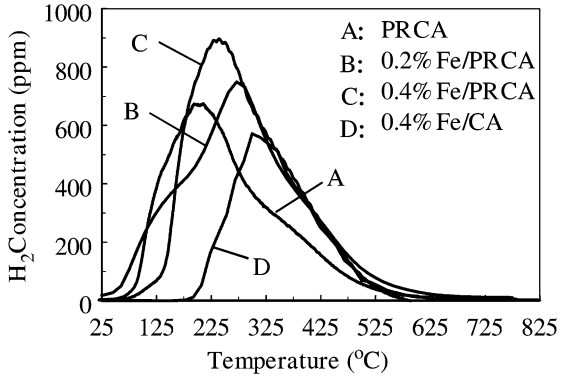

Fig. 4. H_2 temperature-programmed desorption (TPD) response curves obtained over the PRCA, 0.2 and 0.4 wt% Fe/PRCA, and 0.4 wt% Fe/CA solids. $T_{ads} = 25\,^\circ$C; $W = 0.3$ g; $\beta = 30\,^\circ$C/min; $Q_{He} = 30$ NmL/min.

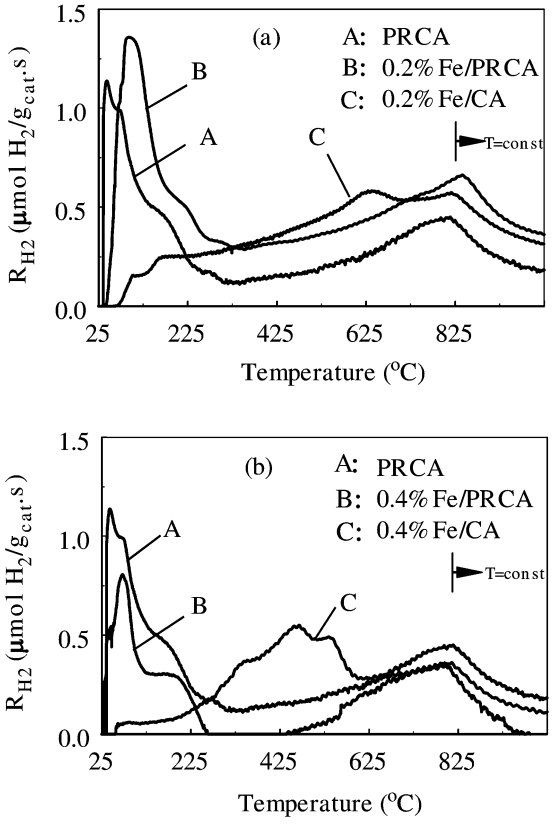

Fig. 5. Temperature-programmed reduction (TPR) traces obtained in 2% H_2/He gas flow over (a) PRCA (curve A), 0.2 wt% Fe/PRCA (curve B), and 0.2 wt% Fe/CA (curve C) solids; (b) PRCA (curve A), 0.4 wt% Fe/PRCA (curve B), and 0.4 wt% Fe/CA (curve C) solids. $W = 0.3$ g; $\beta = 30\,^\circ$C/min; $Q_{H_2/He} = 30$ NmL/min.

whereas the peak at 427 °C was ascribed to a second reduction step [44],

$$Fe_3O_4 + 4H_2 \rightarrow 3Fe^0 + 4H_2O. \quad (8)$$

The results of Fig. 5 demonstrate that adding 0.2 or 0.4 wt% Fe in the PRCA solid caused the TPR trace of rhodium and palladium oxides to shift to higher temperatures. In particular, for 0.2 wt% Fe (Fig. 5a), the T_M shifted from 45 to 85 °C, with a similar behavior seen for the shoulder of this peak. The same behavior was also observed for 0.4 wt% Fe (Fig. 5b). Furthermore, the amount of H_2 consumed up to 225 °C in the TPR traces of Fig. 5, attributed mainly to reduction of PdO, decreased substantially by increasing the Fe loading from 0.2 to 0.4 wt%. In addition, the total amount of H_2 consumed in the 25–825 °C range increased by 60% after the addition of 0.2 wt% Fe in PRCA (685 vs. 1096 μmol-H/g_{cat}; see Fig. 5a), but decreased substantially after the addition of 0.4 wt% Fe (392 μmol-H/g_{cat}; see Fig. 5b). These results are in harmony with the XPS results presented next, which suggest deposition of Fe on the Pd surface or in intimate contact with the latter, and also with the OSC measurements, which showed a decrease in the overall redox performance of PRCA when 0.4 wt% Fe was deposited on the ceria–alumina surface (Fig. 1). On the other hand, the TPR trace in the 600–825 °C range was affected only slightly when 0.4 wt% Fe was added in the PRCA solid (Fig. 5b), whereas a significant increase in the amount of reducible oxygen species at temperatures above 600 °C was observed for the 0.2 wt% Fe/PRCA solid. Significant changes occurred in the TPR trace of Fe/CA with increasing Fe loading from 0.2 to 0.4 wt% (compare the curves C in Figs. 5a and 5b). In particular, the amount of H_2 consumed was found to be 744 μmol-H/g for the 0.2 wt% Fe/CA solid and 520 μmol-H/g for the 0.4 wt% Fe/CA solid.

The foregoing remarks point out that iron at 0.2 and 0.4 wt% affects Pd–O, Pd–O–Ce, and Fe–O–Ce bonding in different ways. Even though doping of ceria lattice with Fe^{3+} was reported after calcination at 1400 °C [22], whether this occurred at the calcination temperature of 800 °C used in the present work remains speculative. However, this possibility cannot be excluded at least to a limited extent within the first subsurface layers, given the high dispersion of iron oxide expected in the Fe/PRCA solids.

The H_2 TPR trace of 0.2 wt% Fe/CA (Fig. 5a, curve C) is very broad. In the 450–825 °C range, a peak at 625 °C not seen in the PRCA appeared. A second peak at 810 °C also appeared, but it was larger than that seen in the PRCA. These results indicate that Fe influences the reduction behavior of CeO_2 in the Al_2O_3–CeO_2 support. The TPR trace of 0.4 wt% Fe/CA (Fig. 5b, curve C) was largely different than that obtained over the 0.2 wt% Fe/CA. In particular, a clear broad peak centered at 450 °C not seen in the 0.2 wt% Fe/CA was obtained. In addition, the peak centered at 810 °C also seen in the 0.2 wt% Fe/PRCA (Fig. 5a) was smaller here. Closer observation of the broad reduction peak observed in the 225–625 °C range over the 0.4 wt% Fe/CA solid reveals two shoulders at 300 and 525 °C. As discussed previously, these features are likely associated with reduction of Fe_2O_3 to Fe^0.

3.4. XPS

Fig. 6a presents Pd 3d photoelectron spectra obtained in the PRCA and 0.2 wt% Fe/PRCA solids after exposure to the 20% O_2/He gas mixture at 500 °C for 2 h; Fig. 6b shows the same after exposure to the 10% H_2/He gas mixture at 300 °C for 2 h after oxidation at 500 °C for 2 h. After oxidation of PRCA and 0.2 wt% Fe/PRCA solids, the Pd $3d_{5/2}$ peak appearing at 337.6 eV (Fig. 6a) was attributed to Pd^{2+}, whereas after H_2 reduction, this peak appearing at 335.5 eV (Fig. 6b) was attributed to Pd^0. These results indicate that Pd was fully oxidized and reduced at the applied conditions. Note, however, that in the H_2 reduction of Fe/PRCA, the binding energy of Pd $3d_{3/2}$ peak shifted to a lower value (by 0.4 eV) with respect to the value obtained in the PRCA solid (Fig. 6b), indicating that reduction of Pd^{2+} was greater than that of PRCA. This result was confirmed by the DRIFTS chemisorption of CO studies (see Section 3.5.3). In the Rh $3d_{5/2}$ photoelectron spectra (not shown here), the peak centered at 309.7 eV was assigned to Rh^{3+}, whereas that at 307.2 eV was assigned to Rh^0. The addition of 0.2 wt% Fe in PRCA caused the binding energy of Rh^{3+} to shift to a lower value (309.3 eV) after oxidation. The same behavior was obtained when the 0.2 wt% Fe/PRCA was subjected to the applied reduction conditions. These results demonstrate that iron affects the electronic environment of Pd

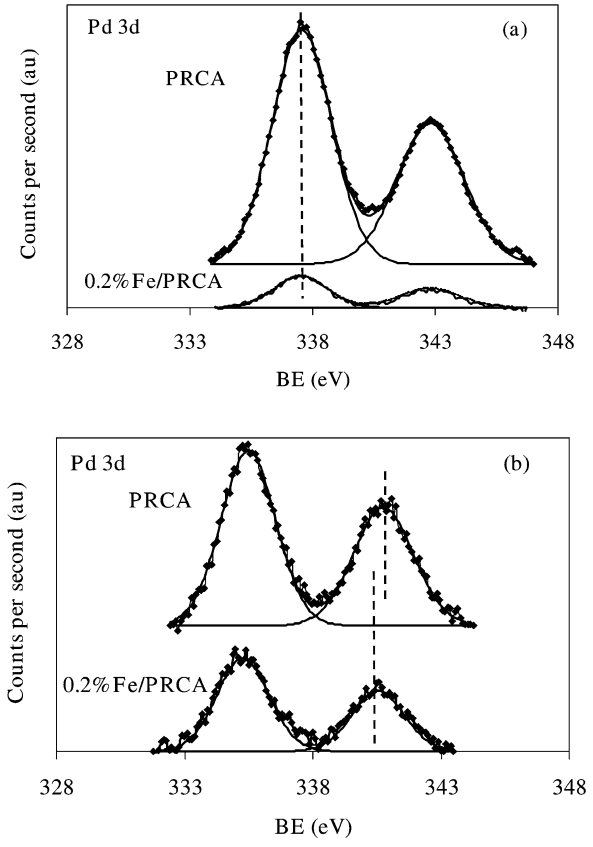

Fig. 6. X-Ray photoelectron spectra of Pd 3d core level obtained over PRCA and 0.2 wt% Fe/PRCA solids after treatment in 20% O_2/He at 500 °C for 2 h (a), and after treatment in 10% H_2/He at 300 °C for 2 h, following oxygen treatment (b).

and Rh surface atoms, in harmony with the H_2 TPD results of Fig. 4 (see Section 3.2).

In the Fe $2p_{3/2}$ photoelectron spectra, the situation is more complicated. After oxidation of the 0.2 wt% Fe/PRCA solid at 500 °C, iron was found only in the Fe^{3+} oxidation state (Fe $2p_{3/2}$ peak at 711.1 eV). After H_2 treatment at 300 °C, complete reduction of Fe^{3+} to Fe^0 was not obtained. Iron appeared instead in two oxidation states, Fe^{3+} (55 at%) and Fe^{2+} (45 at%). This surface iron composition does not correspond exclusively to magnetite ($FeO{\cdot}Fe_2O_3$). The surface after the given reduction conditions applied appeared more enriched in Fe^{2+} than magnetite.

Table 3 reports the surface atom ratios of Ce/Al, Pd/Al, Rh/Al, and Fe/Al for the PRCA and 0.2 wt% Fe/PRCA solids after application of the aforementioned oxidation and reduction treatments. The surface atom ratios of Pd/Al and Rh/Al decreased in the presence of iron; in particular, the Pd/Al ratio decreased by 32% after oxidation and by 41% after reduction. It is logical to suggest that this decrease may be due to deposition of iron/iron oxide crystals on both the alumina and Pd surface and, to a lesser extent, on the Rh surface. The presence of iron in the PRCA also resulted in a lower Ce/Al surface atom ratio after oxidation and reduction treatments. In particular, after reduction, the Ce/Al ratio in the 0.2 wt% Fe/PRCA solid was almost half that in PRCA. These results support the aforementioned observation that Fe was deposited not only on the noble metal surfaces, but also on the support surface, as was also deduced from the H_2 TPR experiments (Fig. 5). Liu et al. [45] reported that Fe oxide can interact strongly with Pt, modifying its electronic surface states. The XPS results of Fig. 6b support that Fe has a similar influence on Pd. A previous study demonstrated that adding a monolayer of Fe_2O_3 (2 wt%) in Pd/CeO_2 significantly increased the rate of the WGS reaction [20]. It was proposed that Fe can transfer oxygen from the iron oxide to the precious metal (Pd), lowering the barrier for oxygen transfer between CeO_2 and Pd, thereby enhancing the WGS reaction rate. The main requirement for this mechanism is that Fe_2O_3 must be in close contact with Pd on the surface of CeO_2. These observations might also help explain the increased OSCC described in Section 3.1.

3.5. In situ DRIFTS studies

3.5.1. Surface oxygen species

The thermal stability and isotopic exchange of surface species formed on oxygen chemisorption at room temperature were studied by in situ DRIFTS. Binuclear oxygen species are involved in oxygen chemisorption and surface diffusion in CeO_2 [46]. These species can be viewed as either intermediates in the activation of oxygen on the ceria surface (storage) or oxygen carriers throughout the oxygen surface diffusion process [46]. It has been reported that oxygen adsorption on ceria at 25 °C resulted in the appearance of a band at 1126 cm^{-1} characteristic of the formation of surface superoxide ($^{16}O_2^-$) species [46–48].

In the present PRCA and 0.2 and 0.4 wt% Fe/PRCA solids, after oxygen chemisorption at 25 °C, a combination of IR bands in the 1250–1025 cm^{-1} range was observed due to the presence of various adsorbed carbonate species. The latter formed as a result of CO_2 impurities in the 3% O_2/Ar gas adsorption mixture prepared in situ (using mass flow control valves) in a flow panel. When preparing this mixture, only the Ar carrier gas was passed through oxygen and water traps. Therefore, spectrum deconvolution (curve fitting) was necessary to correctly quantify the $^{16}O_2^-$ superoxide band and the corresponding bands of the oxygen isotopic species. Fig. 7a presents the DRIFTS spectrum (in K-M units) recorded for the 0.2 wt% Fe/PRCA solid

Table 3
Surface atom ratios of Ce, Pd, Rh and Fe with respect to Al in the PRCA and 0.2 wt% Fe/PRCA catalysts derived from XPS analyses

Catalyst	Pretreatment	Ce/Al	Pd/Al	Rh/Al	Fe/Al
PRCA	O_2/500 °C/2 h	0.071	0.038	0.0023	–
	H_2/300 °C/2 h	0.116	0.032	0.0023	–
0.2 wt% Fe/PRCA	O_2/500 °C/2 h	0.069	0.026	0.002	0.046
	H_2/300 °C/2 h	0.059	0.019	0.002	0.042

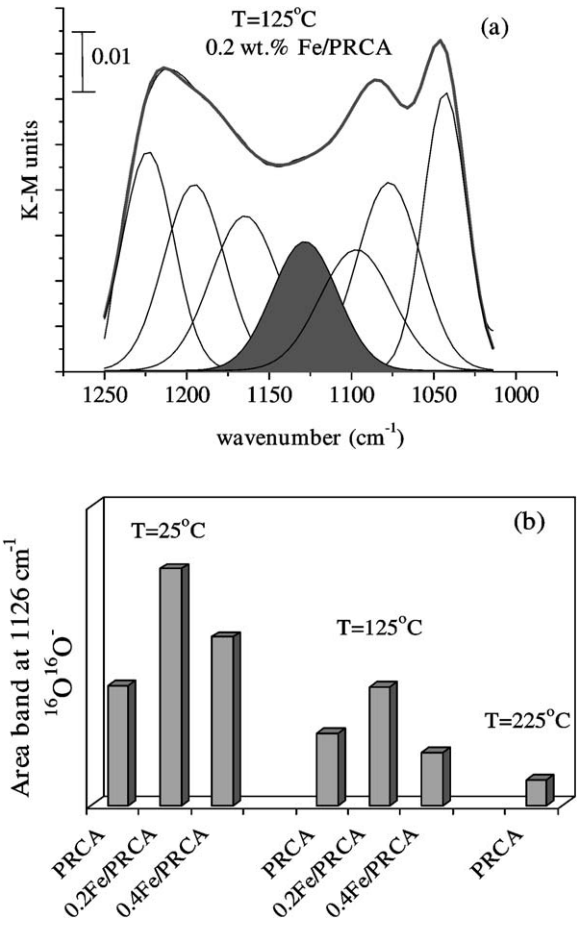

Fig. 7. (a) In situ DRIFTS spectra recorded in the 1250–1000 cm^{-1} range over the 0.2 wt% Fe/PRCA after O_2 adsorption at 25 °C (3% O_2/Ar gas mixture) for 30 min followed by TPD in Ar flow ($T = 125$ °C). After spectrum deconvolution (curve fitting), the superoxide ($^{16}O_2^-$) band centered at 1126 cm^{-1} is marked (shaded area). (b) Area band at 1126 cm^{-1} due to $^{16}O_2^-$ estimated after oxygen chemisorption at 25 °C followed by TPD in Ar flow (125 and 225 °C) over PRCA, 0.2 and 0.4 wt% Fe/PRCA solids.

at 125 °C in the 1250–1000 cm^{-1} range after O_2 adsorption at 25 °C for 30 min followed by TPD in Ar flow. The fresh catalyst sample was first pretreated in 20% O_2/Ar at 550 °C for 2 h, and then cooled quickly to 25 °C in Ar flow. Deconvolution of the spectrum was done after considering the likely bands arising from carbonate adsorbed species and the IR band of superoxide (1126 cm^{-1}) species of interest. Appropriate software (Origin, version 6.0) was used to allow the number of bands (Gaussian band shapes were used) and their position to vary, to obtain the best fitting of the experimental IR spectrum recorded. Similar procedures were also reported for the analysis of complex NO_x adsorption spectra [49]. Fig. 7a shows seven IR bands that best describe the recorded spectrum; these bands are due to (a) monodentate carbonates (1043 cm^{-1} [50,51]), (b) monodentate/polydentate carbonates (1077 cm^{-1} [52,53]), (c) bridged carbonates (1164, 1195, and 1223 cm^{-1} [51,54,55]), (d) polydentate carbonates (1100 cm^{-1} [52,53]), and superoxides on ceria (1126 cm^{-1} [46,48]). The area of the latter band is shaded in Fig. 7a. IR bands due to superoxide species (1100–900 cm^{-1}) have also been reported for various other metal oxides [56].

By increasing the temperature under Ar flow (TPD run), the amount of adsorbed $^{16}O_2^-$ species was significantly decreased, with no superoxide species detected above 250 °C. Superoxide species are characterized as "virtual" intermediates in the reoxidation of CeO_{2-x}, where electrons are progressively transferred from the solid to the dioxygen molecule [57],

$$O_{2gas} \xrightarrow{1} O_{2ads} \xrightarrow{2} O_{2ads}{}^{-}(\text{superoxide}) \xrightarrow{3} O_{2ads}{}^{2-}(\text{peroxide}) \xrightarrow{4} 2O_{ads}{}^{-} \xrightarrow{5} 2O_{lattice}{}^{2-}. \quad (9)$$

Increasing temperature has been suggested to increase the rate of desorption and transformation of superoxide species into O_2^{2-}, O^-, and $O_{lattice}^{2-}$ according to the reaction path given above and the results of previous studies [58].

Fig. 7b presents the area band at 1126 cm^{-1} associated with $^{16}O_2^-$ species, the thermal stability of which was recorded under TPD in Ar flow at 25, 125, and 225 °C for the three solids investigated. IR bands recorded at 25 °C correspond to the end of the oxygen chemisorption step, followed by a 5-min Ar purge. The 1126 cm^{-1} band increased significantly after deposition of 0.2 wt% Fe in PRCA. In contrast, the addition of 0.4 wt% Fe did not result in any further increase in $^{16}O_2^-$ concentration on the ceria surface; rather, a decrease was obtained. As discussed later in the paper (Section 3.5.2), the increased Fe loading at the level of 0.4 wt% weakened the bond between superoxide and the ceria surface, partially explaining the decreased population of this species compared with 0.2 wt% Fe/PRCA solid. At 225 °C, only the PRCA solid surface populated a small amount of superoxide species (Fig. 7b). These results illustrate that Fe, particularly at 0.2 wt%, largely promoted the population of superoxide species on ceria.

To the best of our knowledge, no previous studies have addressed the issue of whether superoxides can also be formed on Fe_2O_{3-x}. We propose that the amount of iron oxide present on the ceria surface regulates the bond strength and thermal stability of superoxides and that the presence of iron oxide does not create more oxygen vacancy sites (potential superoxide adsorption sites) in ceria.

Descorme et al. [46] found a good correlation of the OSC measured at 400 °C on $Ce_xZr_{1-x}O_2$ with the population of superoxide species at 25 °C. They concluded that such species are involved in the oxygen transport and storage on ceria. In the present work, the increased OSC with increasing Fe loading (wt%) in PRCA is in good agreement with the increase of the superoxide IR band, supporting the interpretations given earlier [46].

3.5.2. Oxygen isotopic exchange

After performing oxygen adsorption and exchange at 25 °C (see Section 2.5), the superoxide species $^{16}O_2^-$, $^{16}O^{18}O^-$, and $^{18}O_2^-$ potentially could be observed. Based on earlier studies on ^{18}O exchange in ceria [47,58,59], characteristic stretching vibrational frequencies for $^{16}O^{18}O^-$ and $^{18}O_2^-$ would be expected at around 1094 and 1062 cm^{-1}, respectively. Two types of oxygen-exchange mechanisms on metal oxide surfaces have been suggested [60,61]. The first of these, termed *simple heteroexchange*, involves the participation of only one oxygen atom of the oxide according to the following steps:

$$^{18}O^{18}O(g) + {}^{16}O_s \Leftrightarrow {}^{18}O^{16}O(g) + {}^{18}O_s \quad (10)$$

and

$$^{18}O^{16}O(g) + {}^{16}O_s \Leftrightarrow {}^{16}O_2(g) + {}^{18}O_s. \quad (11)$$

The second mechanisms, *multiple heteroexchange*, involves the participation of two oxygen atoms of the oxide according to the following steps:

$$^{18}O^{18}O(g) + {}^{16}O^{16}O_s \Leftrightarrow {}^{16}O_2(g) + {}^{18}O^{18}O_s, \quad (12)$$

$$^{18}O^{16}O(g) + {}^{16}O^{16}O_s \Leftrightarrow {}^{16}O_2(g) + {}^{16}O_s + {}^{18}O_s, \quad (13)$$

and

$$^{18}O^{16}O(g) + {}^{18}O^{18}O_s \Leftrightarrow {}^{18}O_2(g) + {}^{16}O_s + {}^{18}O_s. \quad (14)$$

Fig. 8 presents the evolution of IR bands of adsorbed $^{18}O_2^-$ species at 1062 cm^{-1} and of adsorbed $^{16}O_2^-$ species at 1126 cm^{-1} [47,58], respectively, after 2 and 10 min of treating

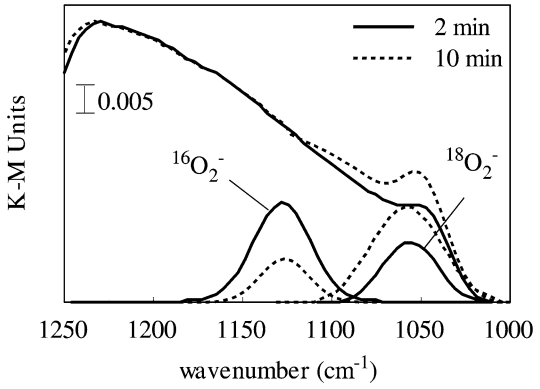

Fig. 8. In situ DRIFTS spectra recorded in the 1250–1000 cm^{-1} range after 2 (—) and 10 (- - -) min of exchange of adsorbed $^{16}O^{16}O^-$ species with gaseous $^{18}O_2$ over the PRCA solid at 25 °C. The evolution of IR bands at 1062 cm^{-1} ($^{18}O_2^-$) and 1126 cm^{-1} ($^{16}O_2^-$) obtained after deconvolution (curve fitting) was performed is indicated.

the PRCA solid at 25 °C in the 3 mol% $^{18}O_2$/He gas mixture. A rapid increase in the 1062 cm^{-1} IR band occurred after 2 min of exchange, but no further development was observed after 10 min of exchange. At the same time, the IR band at 1126 cm^{-1} decreased. The recorded spectra in the 1250–1000 cm^{-1} range after 2 (—) and 10 (- - -) min of exchange (before deconvolution) are also shown. Clearly, the only part of the IR band exhibiting a distinct increase is that due to the $^{18}O_2^-$ superoxide species. This result confirms the accuracy of the deconvolution analysis performed earlier. Note that exchange of $^{18}O_2$(g) with carbonate-adsorbed species at 25 °C did not occur. Using a band centered at around 1094 cm^{-1} ($^{16}O^{18}O^{-1}$) in the deconvolution analysis shown in Fig. 8 could not produce the observed experimental spectrum in the 1250–1000 cm^{-1} range, indicating that significant oxygen exchange occurred via the multiple heteroexchange mechanism [Eq. (12)]. After conducting $^{18}O_2$ isotope-exchange studies over CeO_2, MgO, Al_2O_3, ZrO_2, and CeO_2–Al_2O_3, Martin et al. [58] concluded that simple heteroexchange is the principal mechanism of oxygen exchange on alumina, but that both simple and multiple exchanges occur on ceria. On CeO_2–Al_2O_3, the oxygen exchange process is more complex, and both mechanisms can occur equally well.

Figs. 9a and 9b compare the development of the area band due to $^{18}O_2^-$ and $^{16}O_2^-$ adsorbed species, respectively, obtained in PRCA and 0.2 and 0.4 wt% Fe/PRCA solids after 2, 5, and 10 min of treatment in $^{18}O_2$/He at 25 °C. Adding 0.2 wt% Fe in PRCA significantly increased the formation of $^{18}O_2^-$ species compared with that in PRCA (Fig. 9a), while at the same time enhancing the depletion of $^{16}O_2^-$ (Fig. 9b). In contrast, adding 0.4 wt% Fe in PRCA resulted in a significant decrease in the amount of exchangeable O_2^- adsorbed species compared with that obtained from adding 0.2 wt% Fe/PRCA solid; however, the population of these species was still apparently higher than that in PRCA solid. These results seem to not support the view that Fe promotes the population of adsorbed $^{16}O_2^-$ species by creating oxygen vacancy sites (i.e., adsorption sites of binuclear oxygen species). It seems rather reasonable to suggest that an optimum Fe loading exists that enhances the overall rate of the oxygen multiple heteroexchange mechanism. According to the XPS (Section 3.4), TPR (Section 3.3), and TPD (Section 3.2) studies, the presence of Fe alters the electronic environment of Pd, Rh, and CeO_2 support to some extent, likely enhancing oxygen diffusion on ceria and decreasing the bond strength between binuclear oxygen species and the ceria surface. Comparing the OSC results shown in Figs. 1 and 9 may suggest that binuclear oxygen species participate in the oxygen storage and release processes in PRCA and Fe/PRCA solids, as has also been reported for $Ce_xZr_{1-x}O_2$ solids [46].

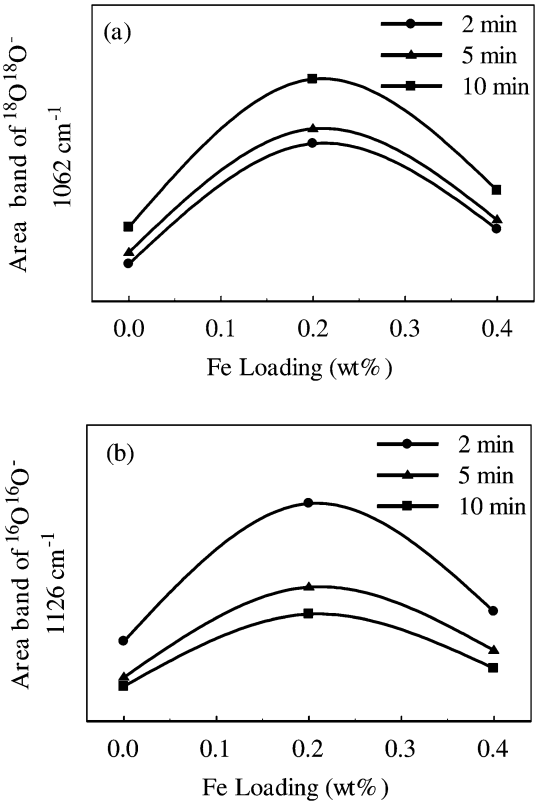

Fig. 9. Comparison of IR area bands at 1062 cm^{-1} ($^{18}O^{18}O^-$) (a) and 1126 cm^{-1} ($^{16}O^{16}O^-$) (b) as a function of Fe loading (x = 0.0, 0.2 and 0.4 wt%) and time in oxygen isotopic exchange at 25 °C recorded over the PRCA solids.

3.5.3. CO and NO chemisorption at 25 °C

Fig. 10a presents in situ DRIFTS spectra recorded after 30 min of CO adsorption at 25 °C on PRCA and 0.2 wt%

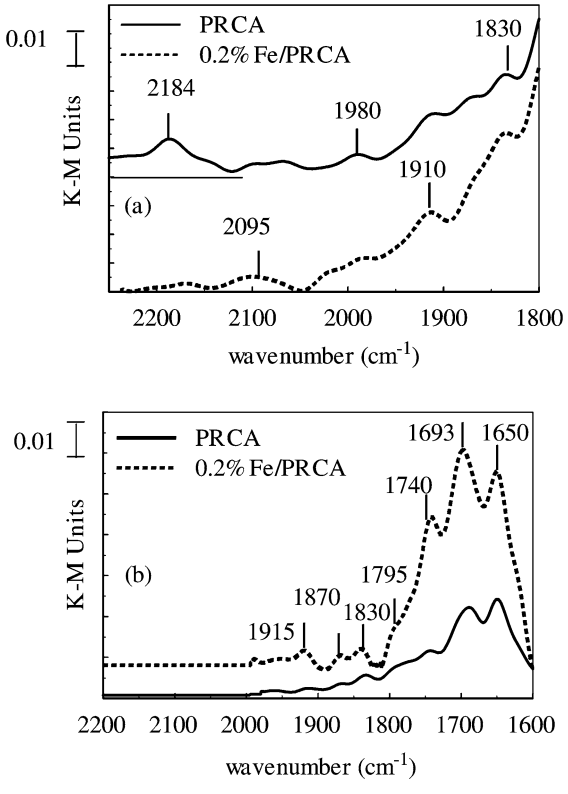

Fig. 10. In situ DRIFTS spectra recorded after (a) CO, and (b) NO chemisorption at 25 °C over PRCA (—) and 0.2 wt% Fe/PRCA (- - -) solids. Adsorption conditions: 5% CO/Ar or 1% NO/Ar, Q = 30 NmL/min, W = 30 mg (KBr/catalyst = 10/1 w/w). Pretreatment conditions: Oxidation (20% O_2/Ar) at 550 °C for 2 h followed by reduction (10% H_2/Ar) at 300 °C for 2 h.

Fe/PRCA solids. It has been reported [62–66] that the stretching ν(C–O) frequency is >2170 cm^{-1} for the M^{2+}–CO adsorbed species, 2160–2120 cm^{-1} for M^{+}–CO, and <2100 cm^{-1} for M–CO (M^{2+} and M^{+}, metal cations; M, reduced metal surface atoms). Weak bands in the 1800–1000 cm^{-1} range (not shown in Fig. 10a) due to various carbonate-like species adsorbed on CeO_2–Al_2O_3 were observed [51,67]. The band at 2184 cm^{-1} (Fig. 10a) can be assigned to CO adsorbed on cationic Pd^{2+} species. This band was practically absent in the IR spectrum obtained with the 0.2 wt% Fe/PRCA solid. This is in agreement with the present XPS studies (Fig. 6b), which demonstrated that iron in PRCA increases the number of Pd^0 surface atoms compared with PRCA after H_2 reduction. A small IR band at 2095 cm^{-1} (Fig. 10a) appearing in both solids can be assigned to linearly adsorbed CO on Pd^0 [68–71]. The IR band at 1980 cm^{-1} observed in both solids corresponds to adsorbed CO-forming islands on the Pd surface [72] (every CO molecule is bridged with two Pd^0 atoms). The IR band at 1910 cm^{-1} is assigned to isolated Pd^0–CO–Pd^0 [73]; that at 1830 cm^{-1}, to bridged CO species on reduced Rh [74,75]. The concentrations of the latter two adsorbed species appear to be greater in 0.2 wt% Fe/PRCA than in PRCA (Fig. 10a) solid, in agreement with the fact that Fe promotes the reduced state of Pd and Rh in the Fe/PRCA solid, according to our XPS studies (Fig. 6b).

Fig. 10b presents in situ DRIFTS spectra recorded after 30 min of NO adsorption at 25 °C on PRCA and 0.2 wt% Fe/PRCA solids. The IR band at 1740 cm^{-1} was assigned to linear NO on Pd^0 [76], where its intensity becomes larger in the 0.2 wt% Fe/PRCA solid. A similar result was also found for CO chemisorption (Fig. 10a). The IR bands at 1693 and 1650 cm^{-1} were assigned to bent Pd–NO^- [22] and to linear Pd–NO^- and Rh–NO^- species [76], respectively. A shoulder at 1795 cm^{-1} corresponded to NO adsorbed on Pd^{2+} [76], the intensity of which hardly changed on the addition of 0.2 wt% Fe in PRCA solid. These results are in harmony with the XPS results (Fig. 6b), in which the presence of Fe in the PRCA solid further facilitated the presence of a higher concentration of reduced Pd^0 after H_2 treatment at 300 °C. Note that NO can oxidize Pd^0 to Pd^{2+} during adsorption at 25 °C by forming N_2O [77,78]. The fact that the shoulder at 1795 cm^{-1} was rather small implies the small extent of this route. The very small IR bands obtained at 1830, 1870, and 1915 cm^{-1} in the 0.2 wt% Fe/PRCA solid have been assigned to mononitrosyl $Fe^{2+}(NO)$, dinitrosyl $Fe^{2+}(NO)_2$, and polynitrosyl $Fe^{2+}(NO)_n$ species, respectively [79]. As seen in Fig. 10, the intensities of all previously mentioned IR bands increase when 0.2 wt% Fe is deposited in PRCA, demonstrating that Fe affects the chemisorptive properties of Pd and Rh with respect to NO and CO chemisorption. At the same time, Fe creates new active sites for adsorption and reduction of NO and adsorption and oxidation of CO and C_3H_6, according to recent results obtained in our laboratory, which we will report elsewhere [80].

4. Conclusion

The following conclusions can be derived from the results of the present work:

(i) Fe deposited on a model TWC (Pd–Rh/CeO_2–Al_2O_3) in amounts between 0.1 and 0.3 wt% does not reduce the oxygen storage capacity (OSC) of the catalyst. Instead, Fe increases the catalyst's OSC up to 40% in the 500–850 °C range compared with the catalyst uncontaminated with Fe. When the amount of Fe deposited increases to 0.4 wt%, the OSC decreases but still remains larger than the OSC measured over the uncontaminated with Fe catalyst.

(ii) The results of H_2 TPD, H_2 TPR, and XPS studies indicated that iron in the Fe/PRCA solid was partly deposited on Pd and Rh, as well as on the ceria component of support. An electronic interaction was formed between noble metals and Fe, which influences the redox properties of Pd and Rh. The latter was also probed by in situ DRIFTS of CO and NO chemisorption. The Ce–O–Ce bond strength was also affected.

(iii) In situ DRIFTS studies indicated that iron significantly favored the formation of superoxide (O_2^-) species on CeO_2 when deposited on the PRCA catalyst at the 0.2 wt% level and also, to a lesser extent, at the 0.4 wt% level. Increasing the Fe loading from 0.2 to 0.4 wt% weakened the bond strength of O_2^- with the ceria surface.

(iv) Oxygen $^{18}O_2$ isotopic exchange performed on the x wt% Fe/Pd–Rh/CeO_2–Al_2O_3 ($x = 0, 0.2, 0.4$) catalysts at 25 °C demonstrated that oxygen exchange proceeded mainly via the multiple heteroexchange mechanism. Furthermore, adding Fe in the 0.2–0.4 wt% range influenced the rate of binuclear $^{18}O_2^-$ species formation.

Acknowledgments

The authors thank the European Union (contract G5RD-CT-2000-00376), the Cyprus Research Promotion Foundation (ATKA project), and the Research Committee of the University of Cyprus for financial support. They also thank Professor José Garcia Luis Fierro (ICP/CSIC, Madrid) for performing the XPS measurements.

References

[1] C. Larese, F.C. Galisteo, M.L. Granados, R. Mariscal, J.L.G. Fierro, M. Furió, R.F. Ruiz, Appl. Catal. B: Environ. 40 (2003) 305, and references therein.
[2] P.S. Lambrou, C.N. Costa, S.Y. Christou, A.M. Efstathiou, Appl. Catal. B: Environ. 54 (2004) 237, and references therein.
[3] M.J. Rokosz, A.E. Chen, C.K. Lowe-Ma, A.V. Kucherov, D. Benson, M.C. Paputa Peck, R.W. McCabe, Appl. Catal. B: Environ. 33 (2001) 205, and references therein.
[4] U. Lassi, R. Polvinen, S. Suhonen, K. Kallinen, A. Savimäki, M. Harkonen, M. Valden, R.L. Keiski, Appl. Catal. A: Gen. 263 (2004) 241.
[5] M. Hietikko, U. Lassi, K. Kallinen, A. Savimäki, M. Härkönen, J. Pursiainen, R.S. Laitinen, R.L. Keiski, Appl. Catal. A: Gen. 277 (2004) 107.
[6] R.K. Usmen, R.W. McCabe, G.W. Graham, W.H. Weber, C.R. Petrs, H.S. Gandhi, SAE Paper no. 922336 (1992).
[7] T. Tabata, K. Baba, H. Kawashima, Appl. Catal. B: Environ. 7 (1995) 19.
[8] C.H. Bartholomew, Appl. Catal. A: Gen. 212 (2001) 17.
[9] M. Waqif, P. Bazin, O. Saur, J.C. Lavalley, G. Blanchard, O. Touret, Appl. Catal. B: Environ. 11 (1997) 193.
[10] V. Meeyoo, D.L. Trimm, N.W. Cant, Appl. Catal. B: Environ. 16 (1998) L101.
[11] G.C. Joy, F.S. Molinaro, E.H. Homeier, SAE Paper no. 852099 (1985).

[12] W.B. Williamson, J. Perry, R.L. Goss, H.S. Gandhi, R.E. Beason, SAE Paper no. 841406 (1984).
[13] P.S. Lambrou, S.Y. Christou, A.P. Fotopoulos, F.K. Foti, T.N. Angelidis, A.M. Efstathiou, Appl. Catal. B: Environ. 59 (2005) 1.
[14] G.C. Koltsakis, A.M. Stamatelos, Prog. Energy Combust. Sci. 23 (1997) 1.
[15] T.N. Angelidis, S.A. Sklavounos, Appl. Catal. A: Gen. 133 (1995) 121.
[16] T.N. Angelidis, V.G. Papadakis, Appl. Catal. B: Environ. 12 (1997) 193.
[17] R.F. Ruiz, M. Furió, F.C. Galisteo, C. Larese, M.L. Granados, R. Mariscal, J.L.G. Fierro, Anal. Chem. 74 (2002) 5463.
[18] Y. Sakamoto, K. Higuchi, N. Takahashi, K. Yokota, H. Doi, M. Sugiura, Appl. Catal. B: Environ. 23 (1999) 159.
[19] H. Ohtsuka, Catal Lett. 87 (2003) 179.
[20] X. Wang, R.J. Gorte, Appl. Catal. A: Gen. 247 (2003) 157.
[21] A. Sirijaruphan, J.G. Goodwin Jr., R.W. Rice, J. Catal. 224 (2004) 304.
[22] V.R. Mastelaro, V. Briois, D.P.F. de Souza, C.L. Silva, J. Eur. Ceram. Soc. 23 (2003) 273.
[23] K. Yamazaki, N. Takahashi, H. Shinjoh, M. Sugiura, Appl. Catal. B: Environ. 53 (2004) 1.
[24] H.C. Yao, Y.F. Yu Yao, J. Catal. 86 (1984) 254.
[25] C.N. Costa, S.Y. Christou, G. Georgiou, A.M. Efstathiou, J. Catal. 219 (2003) 259.
[26] C.N. Costa, T. Anastasiadou, A.M. Efstathiou, J. Catal. 194 (2000) 250.
[27] A.M. Efstathiou, Ph.D. Thesis, University of Connecticut, USA, 1989.
[28] C.D. Wagner, L.E. Davis, M.V. Zeller, J.A. Taylor, R.H. Raymond, L.H. Gale, Surf. Interface Anal. 3 (1981) 211.
[29] S.Y. Christou, C.N. Costa, A.M. Efstathiou, Top. Catal. 30/31 (2004) 325.
[30] L.Z. Gao, C.T. Au, J. Catal. 189 (2000) 1.
[31] L. Xu, G.D. Lei, W.M.H. Sachtler, R.D. Cortright, J.A. Dumesic, J. Phys. Chem. 97 (1993) 11517.
[32] D. Wang, T.B. Flanagan, R. Balasurbramaniam, J. Alloys Compd. 356 (2003) 3.
[33] O. Kubaschewski, Iron Binary Phase Diagrams, Springer-Verlag, Berlin, 1982.
[34] P. Fornasiero, R. Di Monte, G.R. Rao, J. Kašpar, S. Meriani, A. Trovarelli, M. Graziani, J. Catal. 151 (1995) 168.
[35] E. Rogemond, R. Fréty, V. Perrichon, M. Primet, S. Salasc, M. Chevrier, C. Gauthier, F. Mathis, J. Catal. 169 (1997) 120.
[36] J.G. Nunan, W.B. Williamson, H.J. Robota, SAE Paper no. 960798 (1996).
[37] J.G. Nunan, SAE Paper no. 970467 (1997).
[38] P. Vidmar, P. Fornasiero, J. Kašpar, G. Gubitosa, M. Graziani, J. Catal. 171 (1997) 160.
[39] H. Lieske, J. Volter, J. Phys. Chem. 89 (1985) 1841.
[40] T.C. Chang, J.J. Chen, C.T. Yeh, J. Catal. 96 (1985) 51.
[41] H.Y. Lin, Y.W. Chen, C. Li, Thermochim. Acta 400 (2003) 61.
[42] O.J. Wimmers, P. Arnoldy, J.A. Moulijn, J. Phys. Chem. 90 (1986) 1331.
[43] E.E. Unmuth, L.H. Schwartz, J.B. Butt, J. Catal. 63 (1980) 404.
[44] G. Munteanu, L. Ilieva, D. Andreeva, Thermochim. Acta 291 (1997) 171.
[45] X. Liu, O. Korotkikh, R. Farrauto, Appl. Catal. A: Gen. 226 (2002) 293.
[46] C. Descorme, Y. Madier, D. Duprez, J. Catal. 196 (2000) 167, and references therein.
[47] C. Li, K. Domen, K.I. Maruya, T. Onishi, J. Am. Chem. Soc. 111 (1989) 7683.
[48] S. Coluccia, A.J. Tench, J. Chem. Soc., Faraday Trans. 1 79 (1983) 1881.
[49] B. Westerberg, E. Fridell, J. Mol. Catal. A: Chem. 165 (2001) 249.
[50] T. Shido, Y. Iwasawa, J. Catal. 136 (1992) 493.
[51] C. Li, Y. Sakata, T. Arai, K. Domen, K. Maruya, T. Onishi, J. Chem. Soc., Faraday Trans. 1 85 (1989) 929.
[52] C. Binet, A. Jadi, J.C. Lavalley, J. Chim. Phys. 89 (1992) 1779.
[53] M. Daturi, C. Binet, J.C. Lavalley, G. Blanchard, Surf. Interface Anal. 30 (2000) 273.
[54] H. Zhu, Z. Qin, W. Shan, W. Shen, J. Wang, J. Catal. 225 (2004) 267.
[55] F.C. Meunier, D. Tibiletti, A. Goguet, D. Reid, R. Burch, Appl. Catal. A: Gen. 289 (2005) 104.
[56] J. Ryczkowski, Catal. Today 68 (2001) 263.
[57] M. Che, A.J. Tench, Adv. Catal. 31 (1982) 77.
[58] D. Martin, D. Duprez, J. Phys. Chem. 100 (1996) 9429.
[59] C. Li, K. Domen, K.I. Maruya, T. Onishi, J. Catal. 123 (1990) 436.
[60] J. Novakova, Catal. Rev. 4 (1970) 77.
[61] G.K. Boreskov, Adv. Catal. 15 (1964) 285.
[62] Y.A. Lokhov, A.A. Davydov, Kinet. Katal. 21 (1980) 1093.
[63] M. Bensalem, J.C. Muller, D. Tessier, F.B. Verduraz, J. Chem. Soc., Faraday Trans. 1 92 (1996) 3233.
[64] D. Tessier, A. Rakai, F.B. Verduraz, J. Chem. Soc., Faraday Trans. 1 88 (1992) 741.
[65] T. Jin, Y. Zhou, G.J. Mains, J.M. White, J. Phys. Chem. 91 (1987) 5931.
[66] F. Bozon-Verduraz, A. Bensalem, J. Chem. Soc., Faraday Trans. 1 90 (4) (1994) 653.
[67] S. Hilaire, X. Wang, T. Luo, R.J. Gorte, J. Wagner, Appl. Catal. A: Gen. 215 (2001) 271.
[68] M. Fernández-García, A. Martínez-Arias, L.N. Salamanca, J.M. Coronado, J.A. Anderson, J.C. Conesa, J. Soria, J. Catal. 187 (1999) 474.
[69] S. Tsubota, D. Cunningham, Y. Bando, M. Haruta, Stud. Surf. Sci. Catal. 77 (1993) 325.
[70] G.S. Zafiris, R.J. Gorte, J. Catal. 139 (1993) 561.
[71] H. Cordatos, R.J. Gorte, J. Catal. 159 (1996) 112.
[72] P. Hollins, Surf. Sci. Rep. 16 (1992) 51.
[73] R. Craciun, W. Daniell, H. Knözinger, Appl. Catal. A: Gen. 230 (2002) 153.
[74] D.I. Kondarides, Z. Zhang, X.E. Verykios, J. Catal. 176 (1998) 536, and references therein.
[75] C. Force, J.P. Belzunegui, J. Sanz, A.M. Arias, J. Soria, J. Catal. 197 (2001) 192.
[76] K. Almusaiteer, S.S.C. Chuang, J. Catal. 184 (1999) 189.
[77] K. Almusaiteer, S.S.C. Chuang, J. Catal. 180 (1998) 161.
[78] Z. Liu, Y. Fu, J. Tu, M. Meng, Catal. Lett. 81 (3) (2002) 285.
[79] G. Berlier, G. Ricchiardi, S. Bordiga, A. Zecchina, J. Catal. 229 (2005) 127.
[80] P.S. Lambrou, A.M. Efstathiou, Appl. Catal. B: Environ., submitted for publication.